Radiative transfer in ocean turbulence and its effect on underwater light field

Citation: Xu, Zao, Xin Guo, Lian Shen, and Dick K. P. Yue. "Radiative Transfer in Ocean Turbulence and Its Effect on Underwater Light Field." Journal of Geophysical Research: Oceans 117, no. C7 (March 22, 2012): n/a–n/a.

As Published: http://dx.doi.org/10.1029/2011JC007351

Publisher: American Geophysical Union (AGU)

Persistent URL: http://hdl.handle.net/1721.1/120314

Version: Final published version: final published article, as it appeared in a journal, conference proceedings, or other formally published context

Radiative transfer in ocean turbulence and its effect on underwater light field

Zao Xu,[1] Xin Guo,[2] Lian Shen,[2] and Dick K. P. Yue[1]

Received 1 June 2011; revised 22 November 2011; accepted 30 January 2012; published 22 March 2012.

[1] Turbulence in the upper ocean generates fluctuations in temperature and salinity, which result in variations in inherent optical properties (IOPs) and further change the underwater light field. A simulation-based study is performed for the radiative transfer (RT) of natural light in the turbulent flows in the upper ocean. For a canonical problem of turbulent shear flow interacting with the sea surface with and without surface waves, large-eddy simulations are performed for fluid motions and the transport of temperature and salinity. Based on the resolved turbulence temperature and salinity fields, IOP variations are quantified, and the inhomogeneous RT equation is then simulated using a Monte Carlo method. Through the simulations of a variety of cases with different flow, temperature, and salinity conditions, the statistics of downwelling irradiance are quantified and analyzed. It is found that the vertical profile of the mean downwelling irradiance is mainly determined by the vertical structure of the mean values of the IOPs; and turbulence effect is manifested in the horizontal variations of the downwelling irradiance. The magnitude of the irradiance variation is governed by the differences in the temperature and salinity between their values at the surface and in the deep region. In the presence of surface waves, the irradiance variation is enhanced due to the surface deformation, which is also largely affected by wave–turbulence interaction. The LES and inhomogeneous RT simulation may provide a useful tool for the characterization of upper-ocean turbulence processes based on underwater RT measurements.

Citation: Xu, Z., X. Guo, L. Shen, and D. K. P. Yue (2012), Radiative transfer in ocean turbulence and its effect on underwater light field, *J. Geophys. Res.*, *117*, C00H18, doi:10.1029/2011JC007351.

1. Introduction

[2] The fluctuations of solar irradiance and radiance in the upper ocean have been studied experimentally and theoretically for half a century. Existing analytical and numerical models are based on the assumption that the in-water irradiance and radiance variations are associated with the focusing and defocusing of sunlight at the air–water interface and the light scattering and absorption within the ocean body. Scattering acts like a low-pass filter and smooths out the high frequencies of the light field. The fluctuation magnitude of downwelling irradiance decreases when the single scattering albedo increases. Experimentalists including *Snyder and Dera* [1970], *Dera and Stramski* [1986], *Stramski and Legendre* [1992], and *Gernez and Antoine* [2009] built specific instruments to measure temporal variations of underwater solar irradiance and radiance. Recently, *You et al.* [2009] theoretically investigated the wave-induced irradiance fluctuation with direct simulation. *Shen et al.* [2011] developed an analytical model for the probability distribution of underwater irradiance induced by wind-driven surface waves. Both the above two theoretical studies employed empirical linear wave spectral models and assumed that the solar light propagates in a homogeneous ocean medium. However, it should be noted that wave nonlinearity can sometimes be important and that due to oceanic turbulence, fluctuations of temperature and salinity may cause variations of inherent optical properties (IOPs) to change the solar light field.

[3] Although the light propagation affected by atmospheric turbulence and clouds has been widely studied, less attention has been paid to the turbulence effect on the ocean side. A pioneering work was done by *Chilton et al.* [1969], who investigated the effect of oceanic turbulence on underwater images. *Gilbert and Honey* [1972] also studied this effect and found that the fluctuations in temperature and salinity can be large enough to degrade image quality, especially for coherent light. *Bogucki et al.* [1998, 2004] numerically and experimental studied the effect of refractive index change caused by oceanic turbulence on the scattering coefficient and volume scattering function at near-forward angles. *Bogucki et al.* [2007a] then developed a method to extract the rate of temperature variance dissipation from light scattering measurements; *Bogucki et al.* [2007b] also numerically investigated the effect of turbulence-induced IOP variations on returning lidar signals. Recently, *Lu et al.* [2006] studied

[1]Department of Mechanical Engineering, Massachusetts Institute of Technology, Cambridge, Massachusetts, USA.
[2]Department of Civil Engineering, Johns Hopkins University, Baltimore, Maryland, USA.

0148-0227/12/2011JC007351

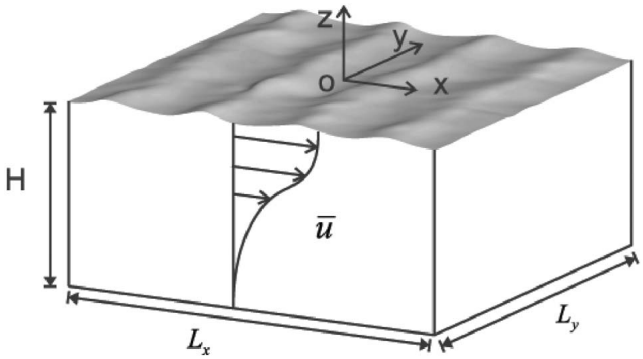

Figure 1. Schematics of the turbulent shear flow in the upper ocean considered in the present study.

the propagation of a partially coherent beam in oceanic turbulence and illustrated the dependence of the normalized root-mean-square (RMS) width of the beam on turbulence. *Korotkova and Farwell* [2011] investigated the effect of oceanic turbulence on the polarization of stochastic beams. The above studies focus on the propagation of fully or partially coherent light beams within the oceanic turbulence. In these cases, the variation of refractive index is the major factor contributing to the distortion of light beams. Both *Lu et al.* [2006] and *Korotkova and Farwell* [2011] used the spectral model of refractive index for the seawater, which was developed by *Nikishov and Nikishov* [2000] with the approximation of single scattering for coherent light.

[4] In oceans under natural conditions, the incoherent solar light is dominant. It has been found that turbulence has relatively weaker effect on incoherent light than on coherent light [*Mobley*, 1994; *Lu et al.*, 2006]. *Duntley* [1974] showed that for solar light, the very small change of refractive index due to turbulence does not significantly affect the distribution of radiant energy in water. The scattering change in turbulent flows was found unimportant to the overall redistribution of radiant energy by *Mobley* [1994]. Nevertheless, it has been observed that turbulence leads to changes in time-averaged volume scattering function. *Honey and Sorenson* [1970] studied the turbulence-induced optical absorption and scattering properties in ocean and found enhancement of forward scattering at very narrow angles. *Bogucki et al.* [1998, 2004] built a theoretical model and reproduced the same behavior of volume scattering function at very small forward scattering angles. Besides the volume scattering function, the dependence of absorption and scattering coefficients and refractive index of pure seawater on temperature and salinity was illustrated in many studies including *Pegau et al.* [1997], *Zhang et al.* [2009], *McNeil* [1977], *Pope and Fry* [1997], and *Quan and Fry* [1995]. The models obtained from their studies are discussed in section 2.2.

[5] With the increasing capability of underwater light sensing, which has become a potential way of passive measurement of upper ocean conditions, it has become possible and worthwhile to quantify the small fluctuations in natural underwater light. Instead of the Maxwell equations with the approximation of single scattering or first-order treatment of multiple scattering, radiative transfer equation (RTE) with spatially dependent absorption and scattering coefficients and phase function has become amenable to solve to yield the solar radiant energy propagation in oceanic and atmospheric turbulence. In general, changes of refractive index in real and imaginary parts are interpreted as the respective changes of scattering and absorption coefficients in the RTE. Recently, derivations of modified RTE accounting for continuously changing refractive index were reported [*Shendeleva and Molloy*, 1999; *Tualle and Tinet*, 2003; *Premaratne et al.*, 2005; *Bal*, 2006]. Their derivations are based on approximation of geometric optics, and the bending effect of light is explicitly expressed in the RTE.

[6] In this paper, we report a simulation based study on the effect of oceanic turbulence on natural underwater light field. We develop numerical models for the large-eddy simulation (LES) of turbulent flows in the upper ocean and the transport of scalars (section 2.1). Based on empirical formula in literatures, we incorporate IOP variations due to temperature and salinity fluctuations (section 2.2) to our radiative transfer simulations. Starting from the general RTE that accounts for refractive index changes, we show the validity of ignoring the refractive index term in the upper ocean environment in Monte Carlo (MC) simulations (section 2.3). In section 3, we show the simulation results of downwelling irradiance with and without dynamic ocean surface waves. Finally, we present the conclusions and discussion in section 4.

2. Numerical Models

2.1. Ocean Turbulence Model

[7] We consider a turbulent shear flow in the upper ocean with the presence of surface waves (Figure 1). The frame of references has axes x, y, and z pointing to the streamwise, spanwise, and vertical directions, respectively. The origin of the coordinate system is located on the undisturbed sea surface.

[8] The governing equations of LES are the filtered momentum equations for incompressible and Newtonian flows

$$\frac{\partial \widetilde{u}_i}{\partial t} + \frac{\partial(\widetilde{u}_i \widetilde{u}_j)}{\partial x_j} = -\frac{1}{\rho}\frac{\partial \widetilde{P}}{\partial x_i} - \frac{\partial \tau_{ij}^{SGS}}{\partial x_j}, \qquad i = 1,\ 2,\ 3, \tag{1}$$

and the filtered continuity equation

$$\frac{\partial \widetilde{u}_i}{\partial x_i} = 0. \tag{2}$$

Here, "$\widetilde{(\cdot)}$" denotes the filtered (i.e., resolved at grid scale) value in LES; $\widetilde{u}_i$ (also denoted as $\widetilde{u}$, $\widetilde{v}$, and $\widetilde{w}$) is the resolved velocity; ρ is the water density; $\widetilde{P}$ is the resolved dynamic pressure; and $\tau_{ij}^{SGS} = \widetilde{u_i u_j} - \widetilde{u}_i \widetilde{u}_j$ is the subgrid-scale (SGS) stress, which represents the effect of turbulence eddies smaller than the grid scale on the resolved motion [*Sagaut*, 2006]. We use the Smagorinsky model [*Smagorinsky*, 1963] to represent τ_{ij}^{SGS} as

$$\tau_{ij}^{SGS} = -2\left(C_u \widetilde{\Delta}\right)^2 \left|\widetilde{\mathcal{S}}\right| \widetilde{\mathcal{S}}_{ij}, \tag{3}$$

where C_u is the Smagorinsky coefficient for velocity; $\widetilde{\Delta}$ is the filter width (which equals to grid size in this study); $\widetilde{\mathcal{S}}_{ij} = (\widetilde{u}_{i,j} + \widetilde{u}_{j,i})/2$ is the filtered strain rate; and $|\widetilde{\mathcal{S}}| = (2\widetilde{\mathcal{S}}_{ij}\widetilde{\mathcal{S}}_{ij})^{1/2}$.

[9] Note that the use of the Smagorinsky model for boundary layer flows requires some caution [see, e.g., *Sagaut*, 2006]. *Shen and Yue* [2001] performed an extensively analysis on the inter-scale energy transfer in turbulent flows with a free surface based on data of direct numerical simulation (DNS) on fine grid, and assessed the performance of SGS models through a priori and a posteriori tests on coarse grid. It is found that it is important to correctly represent the variation of the model coefficient in free-surface turbulent flows, and a dynamic procedure to determine the model coefficient is necessary for capturing the physics of free-surface turbulence. In the present study, we have employed the dynamic Smagorinsky model of *Germano et al.* [1991] and *Lilly* [1992] as well as a particular variant of it, namely the scale-dependent Lagrangian dynamic model [*Bou-Zeid et al.*, 2005]. The latter has two attractive features especially suitable for the present wave–turbulence interaction problem. First, in the dynamic procedure [*Germano et al.*, 1991; *Lilly*, 1992] of determining model coefficient, Lagrangian averaging along fluid paths [*Meneveau et al.*, 1996] is used to overcome the difficulty of lacking homogeneous direction for performing spatial averaging to reduce model coefficient fluctuations (for review, see, e.g., *Meneveau and Katz* [2000]) in the flow field that is heterogeneous due to the presence of waves. Second, the complex disequilibrium turbulence field near the boundary can be better addressed with the scale-dependent treatment of the model coefficient [*Porté-Agel et al.*, 2000]. More discussion on the scale-dependent and Lagrangian dynamic modeling approach can be found in the work of *Bou-Zeid et al.* [2004, 2005]. In the present paper, all the results are based on LES using this model.

[10] At the sea surface, the nonlinear kinematic boundary condition (KBC) is

$$\frac{\partial \eta}{\partial t} + \widetilde{u}\frac{\partial \eta}{\partial x} + \widetilde{v}\frac{\partial \eta}{\partial y} - \widetilde{w} = 0, \qquad \text{at} \qquad z = \eta, \tag{4}$$

where η is the surface elevation. We assume the local wind to be weak and model the air as a region with constant pressure. The nonlinear dynamic boundary conditions (DBCs) at $z = \eta$,

$$\vec{t}_1 \cdot [\widetilde{\sigma}] \cdot \vec{n}^T = 0, \qquad \vec{t}_2 \cdot [\widetilde{\sigma}] \cdot \vec{n}^T = 0, \qquad \vec{n} \cdot [\widetilde{\sigma}] \cdot \vec{n}^T = 0, \tag{5}$$

represent the balance of the stress at the free surface. In equation (5), $\widetilde{\sigma}_{ij} = -(\widetilde{P}/\rho - gz)\delta_{ij} + \tau_{ij}^{SGS}$, where g is the gravitational acceleration and δ_{ij} is the Kronecker delta; t_1 and t_2 are the tangential directions of the sea surface and n is the normal direction of the sea surface pointing from the water to the air. They are expressed as

$$\vec{t}_1 = \frac{(1, 0, \eta_x)}{\sqrt{\eta_x^2 + 1}}, \qquad \vec{t}_2 = \frac{(0, 1, \eta_y)}{\sqrt{\eta_y^2 + 1}}, \qquad \vec{n} = \frac{(-\eta_x, -\eta_y, 1)}{\sqrt{\eta_x^2 + \eta_y^2 + 1}}. \tag{6}$$

At the bottom of the computational domain ($z = -H$) that is deep enough to have negligible effect on the near-surface motion, a shear-free boundary condition is applied as

$$\frac{\partial \widetilde{u}}{\partial z} = \frac{\partial \widetilde{v}}{\partial z} = 0, \qquad \widetilde{w} = 0. \tag{7}$$

In the horizontal directions, we use a periodic boundary condition.

[11] For the transport of a scalar in the flow, the governing equation for the scalar concentration, $\widetilde{\theta}$, is

$$\frac{\partial \widetilde{\theta}}{\partial t} + \frac{\partial \widetilde{u}_j \widetilde{\theta}}{\partial x_j} = -\frac{\partial \Theta_i^{SGS}}{\partial x_i}, \tag{8}$$

where Θ_i^{SGS} representing the subgrid-scale diffusion of the scalar is modeled as

$$\Theta_i^{SGS} = -2\left(C_\theta \widetilde{\Delta}\right)^2 \left|\widetilde{\mathcal{S}}\right| \frac{\partial \widetilde{\theta}}{\partial x_i}. \tag{9}$$

Similar to the velocity field simulation, the Smagorinsky coefficient for the scalar, C_θ, is calculated based on the scale-dependent Lagrangian dynamic model.

[12] Two types of scalars, which respectively correspond to temperature and salinity, are considered here. For the temperature, $\widetilde{T}$, because its turbulence transport is mainly controlled by the heat flux due to air-side processes (e.g., evaporation), its boundary conditions are [*Handler et al.*, 1999; *Kermani et al.*, 2011]

$$\frac{\partial \widetilde{T}}{\partial n} = T'_{\text{surface}}, \quad \text{at} \quad z = \eta, \tag{10}$$

$$\widetilde{T} = T_{\text{deep}}, \quad \text{at} \quad z = -H. \tag{11}$$

In the simulation, we take $T_{\text{deep}} = 5°\text{C}$ and T'_{surface} is adjusted to make the average value of T_{surface} equal to 10°C, 15°C, or 20°C. For the salinity, $\widetilde{S}$, because its turbulence transport process is governed by the concentration difference, the boundary conditions are

$$\widetilde{S} = S_{\text{surface}}, \quad \text{at} \quad z = \eta, \tag{12}$$

$$\widetilde{S} = S_{\text{bottom}}, \quad \text{at} \quad z = -H. \tag{13}$$

We take S_{bottom} = 35 ppt and S_{surface} = 32 ppt, 33 ppt, or 34 ppt. Here, ppt stands for "parts per thousand."

[13] To accurately capture the flow motion under the unsteady sea surface, we use a boundary-fitted grid that follows the surface undulatory motion. An algebraic mapping is used to transform the irregular physical domain bounded by the wave surface into a rectangular computational domain by normalizing z with the distance from the sea surface to the computational domain bottom. The governing equations for the flow, (1) and (2), subject to the boundary conditions are integrated in time with a fractional step method [*Kim and Moin*, 1985]. The surface elevation is advanced in time through the integration of the KBC with a Runge–Kutta

scheme. For the spatial discretization, a pseudo-spectral method is used in the horizontal directions. In the vertical direction, we use a finite-difference method. The details of the numerical schemes and the validations are provided by *Guo and Shen* [2009, 2010] and *Yang and Shen* [2011a, 2011b]. The numerical scheme for the scalar governing equation, (8), is similar to that of the momentum equation, with an additional treatment for the scalar flux to conserve scalar mass and prevent unphysical extrema and oscillations in scalar concentration that sometimes occur due to numerical dispersion and diffusion [*Chamecki et al.*, 2008]. We combine a positive-definite flux limiter [*Skamarock*, 2006] that prevents the occurrence of negative scalar concentration values, and a monotonic flux limiter [*Zalesak*, 1979] that prevents the maxima amplification problem, in a way similar to *Skamarock and Weisman* [2009] and *Wang et al.* [2009].

[14] The size of the computational domain is $L_x \times L_y \times H = 260$ m $\times$ 260 m $\times$ 100 m. In the horizontal directions, an evenly distributed 192-point grid is used. In the vertical direction, we use a 97-point grid that is clustered toward the sea surface to have higher resolution near the surface.

[15] Superposed with small velocity noises as seed for turbulence (and a long-crested wave train if surface wave is considered), the simulation starts with a shear flow with a mean velocity profile

$$\frac{\langle \widetilde{u} \rangle}{U_0} = 0.9988\ \mathrm{sech}^2\left(0.88137\frac{z}{L_0}\right), \tag{14}$$

which is representative of wake flows near the sea surface [*Triantafyllou and Dimas*, 1989]. An Orr-Sommerfeld stability analysis of equation (14) has been performed by *Triantafyllou and Dimas* [1989]. The nonlinear evolution of the mean profile is studied by *Dimas and Triantafyllou* [1994] and *Shen et al.* [2000]. *Shen et al.* [2001, 2004] and *Khakpour et al.* [2011] studied the turbulence structures and scalar field.

[16] In this study, for wave effect, two scenarios are considered. One is that the initial wave train propagates in the same direction as the mean flow; and the other is that they travel in opposite directions. In both scenarios, the wavelength of the wave train is $L^p = 65$ m and the initial wave amplitude is $a^p = 1$ m. In the simulations, the sea surface dynamically interacts with the underlying turbulent flow and, as a result, the wave train is distorted and additional small-amplitude, short waves are generated. In addition to these wave scenarios, cases with a flat surface are also simulated to represent a calm ocean surface.

2.2. Atmosphere and Ocean IOPs Models

[17] We consider the solar light propagating in the atmosphere-ocean system. A plane-parallel geometry is assumed for the atmosphere, which is modeled as a two-layer system based on the Maritime Aerosol Model I (MAR-I) [*Adams and Gray*, 2011]. The upper layer contains continental-type aerosols, and the lower layer contains maritime-type aerosols. Assume τ_c is the optical thickness of the continental haze layer, τ_m is the optical thickness of the maritime haze layer, and τ_r is the optical thickness of the Rayleigh scattering layer. We have

$$\tau_c = 0.025,\ \tau_r = 0.114,\ \omega_0 = 0.957 \tag{15}$$

for the upper layer, and

$$\tau_m = 0.05,\ \tau_r = 0.031,\ \omega_0 = 1 \tag{16}$$

for the lower layer. Here, ω_0 is the single scattering albedo. The volume scattering function for the Rayleigh scattering layer is approximated as the Rayleigh scattering phase function, and the volume scattering function for the continental and maritime haze layers uses the Henyey–Greenstein (HG) phase function.

[18] The case 1 water [*Morel and Prieur*, 1977] is assumed for the ocean model. For simplicity, for most of the cases considered in this study, we assume that the chlorophyll concentration along the depth is uniformly distributed with a value $C = 0.1$ mg m^{-3}, which corresponds to very clear (oligotrophic) water. Empirical models of absorption coefficient $a(T, S, C; \lambda)$, scattering coefficient $b(T, S, C; \lambda)$, and refractive index $n(T, S; \lambda)$ are described below.

2.2.1. Absorption Coefficient

[19] A model for the absorption coefficient $a(T, S, C; \lambda)$ in units of m^{-1} was given by *Haltrin* [1998] as:

$$a(T,S,C;\lambda) = a_w(T,S;\lambda) + a_0^c(\lambda)\left(\frac{C}{C_c^0}\right)^{0.602} + a_f^0 C_f \mathrm{e}^{-k_f\lambda} + a_h^0 C_h \mathrm{e}^{-k_n\lambda}. \tag{17}$$

Here, $a_w(T, S; \lambda)$ is the pure water absorption coefficient in m^{-1} with λ being the wavelength of light in nm; a_0^c is the specific absorption coefficient of chlorophyll in m^{-1}; C is the total concentration of chlorophyll in mg m^{-3}; C_c^0 is a constant with the value $C_c^0 = 1$ mg m^{-3}; $a_f^0 = 35.959$ m^2 mg^{-1} and $a_h^0 = 18.828$ m^2 mg^{-1} are the specific absorption coefficients of fulvic acid and humic acid, respectively; C_f and C_h are respectively the concentrations of fulvic and humic acids, both in mg/m^3; and the two remaining constants in the above equation are $k_h = 0.0189$ nm^{-1} and $k_h = 0.01105$ nm^{-1}. The relations among C, C_f, and C_h are given by *Haltrin* [1998] as

$$C_f = 1.74098 \cdot C \cdot \mathrm{e}^{0.12327\cdot C}, \tag{18}$$

$$C_h = 0.19334 \cdot C \cdot \mathrm{e}^{0.12343\cdot C}. \tag{19}$$

According to *Pegau et al.* [1997], one can write the pure water absorption coefficient a_w as a function of temperature T and salinity S as

$$a_w(T,S;\lambda) = a_w(T_r,0;\lambda) + \Psi_T(T - T_r) + \Psi_S S, \tag{20}$$

where T_r is the reference temperature, and Ψ_T and Ψ_S are coefficients of temperature and salinity, respectively. Their values at different light wavelengths are given in Tables 2 and 4 of *Pegau et al.* [1997].And $a_w(T, 0\ ; \lambda)$ and a_0^c were measured by *Bricaud et al.* [1995], who parameterized a_0^c with the following formula:

$$a_0^c(\lambda) = A(\lambda)C^{B(\lambda)}. \tag{21}$$

Table 1. The Values of $a_w(T, 0; \lambda)$ in Equation (20) and Coefficients $A(\lambda)$ and $B(\lambda)$ Used in Equation (21)

λ(nm)	$a_w(T, 0; \lambda)$	$A(\lambda)$	$B(\lambda)$
400	0.00663	0.0263	0.282
500	0.0204	0.023	0.0321
600	0.2224	0.054	0.092

The values of A and B for representative λ considered in the present study are listed in Table 1. Putting the above equations together, we have the following formula

$$a(T,S,C;\lambda) = a_w(T_r,0;\lambda) + \Psi_T(T-T_r) + \Psi_S S + a_0^c(\lambda)\left(\frac{C}{C_c^0}\right)^{0.602} + a_f^0 C_f \mathrm{e}^{-k_f\lambda} + a_h^0 C_h \mathrm{e}^{-k_n\lambda}. \tag{22}$$

In this study, the total chlorophyll concentration is assumed to be independent of the temperature and salinity.

2.2.2. Scattering Coefficient

[20] For the scattering coefficient $b(T, S, C; \lambda)$ that is in units of m^{-1}, we use the model presented by *Haltrin* [1998] and *Zhang et al.* [2009], which is written as

$$b(T,S,C;\lambda) = b_w(T,S;\lambda) + b_s^0(\lambda)C_s + b_l^0(\lambda)C_l. \tag{23}$$

Here, $b_w(T, S; \lambda)$ is the scattering coefficient of pure water in m^{-1}; $b_s^0(\lambda)$ and $b_l^0(\lambda)$ are respectively the specific scattering coefficients for small and large particular matters, both in units of $\mathrm{m}^2\ \mathrm{g}^{-1}$. The spectral dependence of $b_s^0(\lambda)$ and $b_l^0(\lambda)$ was given by *Kopelevich* [1983] as

$$b_s^0(\lambda) = \left(1.1513\ \mathrm{m}^2\,\mathrm{g}^{-1}\right)\left(\frac{400}{\lambda}\right)^{1.7}, \tag{24}$$

$$b_l^0(\lambda) = \left(0.3411\ \mathrm{m}^2\,\mathrm{g}^{-1}\right)\left(\frac{400}{\lambda}\right)^{0.3}. \tag{25}$$

And C_s and C_l, both in g m^{-1}, are respectively the concentrations of small and large particulate matters and they are determined using the following relations [*Haltrin*, 1998]:

$$C_s = 0.01739 \cdot C \cdot \mathrm{e}^{0.11631\cdot C}, \tag{26}$$

$$C_l = 0.76284 \cdot C \cdot \mathrm{e}^{0.03092\cdot C}. \tag{27}$$

[21] According to *Morel and Prieur* [1977], the scattering coefficient of pure water can be obtained as

$$b_w(T,S;\lambda) = 16.06\left(\frac{\lambda_0}{\lambda}\right)^{4.32}\beta_w(90;T,S;\lambda_0), \tag{28}$$

where λ_0 is the reference wavelength of light; $\beta_w(90; T, S; \lambda_0)$ is the volume scattering function at 90°. The detailed expression of $\beta_w(90; T, S; \lambda_0)$ can be found in equation (2) and Table 1 of *Zhang et al.* [2009]. Putting above formula together, we obtain the scattering coefficient $b(T, S, C; \lambda)$ as

$$b(T,S,C;\lambda) = 16.06\left(\frac{\lambda_0}{\lambda}\right)^{4.32}\beta_w(90;T,S;\lambda_0) + b_s^0(\lambda) \cdot 0.01739 \cdot C \cdot \mathrm{e}^{0.11631\cdot C} + b_l^0(\lambda) \cdot 0.76284 \cdot C \cdot \mathrm{e}^{0.03092\cdot C}. \tag{29}$$

2.2.3. Refractive Index

[22] For the refractive index $n(T, S; \lambda)$, we employ the expression of *McNeil* [1977], who used the data provided by *Austin and Halikas* [1976] to obtain an empirical equation for the refractive index of seawater as a function of light wavelength, temperature, and pressure. In the upper ocean, the influence of pressure on refractive index is very small. Therefore, the empirical equation is simplified as

$$n(T,S;\lambda) = 1.3247 - 2.5\times10^{-6}\,T^2 + S\left(2\times10^{-4} - 8\times10^{-7}T\right) + \frac{3300}{\lambda^2} - \frac{3.2\times10^7}{\lambda^4}. \tag{30}$$

2.2.4. Phase Function

[23] According to *Mobley* [1994], the phase function of the seawater $p(T, S; \Theta; \lambda)$ can be written as a summation of phase functions of different components. Here we consider two components, pure seawater and particles:

$$p(T,S;\Theta;\lambda) = \frac{b_w(T,S;\lambda)}{b(T,S;\lambda)}p_w(\Theta) + \frac{b_p(\lambda)}{b(T,S;\lambda)}p_p(\Theta), \tag{31}$$

where Θ is the scattering angle; $b_w(T, S, \lambda)$ is the depth-independent scattering coefficient of pure seawater; $b_p(\lambda)$ is the particle scattering coefficient; $b = b_p + b_w$ is the total scattering coefficient; $p_w(\Theta)$ is the phase function of pure water, which is expressed as $p_w(\Theta) = 0.06225\,(1 + 0.0835\cos^2\Theta)$; and $p_p(\Theta)$ is the Petzold average particle phase function [*Petzold*, 1972].

2.3. Monte Carlo Method for the Simulation of Inhomogeneous RTE

[24] Considering an incoherent and unpolarized light beam propagating in an isotropic and inhomogeneous medium, its propagation characteristics can be described by a general RTE that considers inhomogeneity in absorption coefficient, scattering coefficient, and refractive index:

$$\mathbf{\Omega}\cdot\nabla I(\mathbf{r};\mathbf{\Omega};\lambda) = -\mathbf{F}I(\mathbf{r};\mathbf{\Omega};\lambda) - c(\mathbf{r};\lambda)I(\mathbf{r};\mathbf{\Omega};\lambda) + b(\mathbf{r};\lambda)\int_{4\pi} p(\mathbf{r};\mathbf{\Omega},\mathbf{\Omega}';\lambda)I(\mathbf{r};\mathbf{\Omega}';\lambda)\mathrm{d}\mathbf{\Omega}' + Q(\mathbf{r};\mathbf{\Omega};\lambda). \tag{32}$$

In the above equation, $I(\mathbf{r}; \mathbf{\Omega}; \lambda)$ in W m^{-2} sr^{-1} nm^{-1} is the radiance, which is a function of location $\mathbf{r}$, solid angle $\mathbf{\Omega}$, and wavelength λ. The solid angle $\mathbf{\Omega}$ in units of sr represents the direction of the light beam. The relation between the solid angle $\mathbf{\Omega}$ and the direction in polar coordinates (θ, ϕ) can be expressed as $\mathrm{d}\Omega = \sin\theta\ \mathrm{d}\ \theta\mathrm{d}\phi$. The wavelength dependence

is defined by averaging the radiance over a small interval $\Delta\lambda$ and imposing $\Delta\lambda \to 0$. ∇ is the gradient in cartesian coordinates; $c(\mathbf{r}; \lambda)$ and $b(\mathbf{r}; \lambda)$ are respectively the attenuation and scattering coefficients; $p(\mathbf{r}; \mathbf{\Omega}, \mathbf{\Omega}'; \lambda)$ is the scattering phase function; and $Q(\mathbf{r}; \mathbf{\Omega}; \lambda)$ are the source terms. All of the above variables are functions of location $\mathbf{r}$. $\mathbf{F}$ is an operator imposed on the radiance to govern the bending of light beam due to the refractive index changes. Several authors reported slightly different forms of $\mathbf{F}$ [*Shendeleva and Molloy*, 1999; *Tualle and Tinet*, 2003; *Bal*, 2006]. But all these forms include the term of the gradient of refractive index, ∇n.

[25] The general RTE with variable refractive index can be solved with a MC method combined with a ray-tracing technique [e.g., *Born and Wolf*, 1970]. In the upper ocean, say, within the top 100 m below the sea surface, the typical magnitude of temperature and salinity variations is $\Delta T \sim 10°\mathrm{C}$ and $\Delta S \sim 2$ ppt [e.g., *Hansen and Thacker*, 1999]. Using the empirical models in section 2.2, for $\lambda \sim 500$ nm, $T \sim 10°\mathrm{C}$, and $S \sim 34$ ppt, say,

$$\frac{\partial n}{\partial T} \sim -10^4 (°\mathrm{C})^{-1}, \ \frac{\partial n}{\partial S} \sim 2 \times 10^{-4} (\mathrm{ppt})^{-1}. \tag{33}$$

Therefore, the gradient of refractive index can be estimated as

$$\nabla n \sim \frac{\left\langle (\Delta n)^2 \right\rangle^{1/2}}{100} \sim \frac{1}{100}\left[\left(\frac{\partial n}{\partial T}\right)^2 (\Delta T)^2 + \left(\frac{\partial n}{\partial S}\right)^2 (\Delta S)^2\right]^{1/2} \sim 1 \times 10^{-5}\,\mathrm{m}^{-1}. \tag{34}$$

[26] As a result, compared with the magnitudes of absorption and scattering coefficient fluctuations, which is about 1×10^{-3} m^{-1}, the effect of the variation of refractive index on the solar radiance energy distribution for natural light is thus two orders of magnitude smaller and can generally be ignored [*Mobley*, 1994]. To simplify the picture, we subsequently focus primarily on the effects of variations of absorption coefficient and volume scattering function on the radiative transfer, and neglect those directly due to variations of the refractive index. The numerical simulations now can be based on the well-known form of RTE in inhomogeneous medium by assuming $\mathbf{F} = 0$, obtaining substantial computational efficiency and simplification.

[27] The MC method is regarded as the most straightforward and physics-orientated method for the prediction of the RT. In this study, we develop a three-dimensional forward MC radiative transfer model to simulate the natural unpolarized light propagation inside the ocean turbulent flow. During each absorption and scattering cycle in the MC simulation, four random numbers, R_i, where $i = 1, 2, 3$, and 4, are generated to determine the photon traveling distance ℓ, scattered polar angle Θ, and azimuthal angle Φ. The traveling distance is obtained by satisfying the condition

$$R_1 = 1 - \exp\left[-\int_0^{\ell} c(\mathbf{r}; \lambda)\right], \tag{35}$$

where the integral is taken in the direction of photon propagation. After traveling by a distance ℓ, it is determined if the photon is scattered ($R_2 \le \omega_0(\mathbf{r}; \lambda)$) or absorbed ($R_2 \ge \omega_0(\mathbf{r}; \lambda)$). If scattered, the scattered polar angle Θ and azimuthal angle Φ are obtained by satisfying

$$R_3 = 2\pi \int_0^{\Theta} p(\theta) \sin\theta \, \mathrm{d}\theta, \tag{36}$$

and

$$\Phi = 2\pi R_4, \tag{37}$$

where for the seawater the scattered azimuthal angle Φ with respect to the incident direction is uniformly distributed over $[0, 2\pi]$.

[28] To validate the MC code, we have compared our simulation with that of *Mobley* [1994]. Consider a water body of case 1 water with variation of IOPs caused by the vertical profile of chlorophyll. The chlorophyll profiles can often be approximated by a Gaussian [*Lewis et al.*, 1983]:

$$C(z) = C_0 + \frac{h}{s\sqrt{2\pi}} \exp\left[-1/2\left(\frac{z - z_{\max}}{s}\right)^2\right]. \tag{38}$$

Here, the parameters C_0, h, s, and $z_{\max}$ are chosen as $C_0 = 0.2$ mg m^{-3}, $h = 144$ mg m^{-2}, $s = 9$ m, and $z_{\max} = -17$ m. The total absorption coefficient $a(z; \lambda)$ was obtained by *Morel* [1991] as

$$a(\lambda) = \left[a_w(\lambda) + 0.06 a_c^*(\lambda) C^{0.65}\right]\left[1 + 0.2\exp(-0.014(\lambda - 400))\right], \tag{39}$$

where $a_c^*(\lambda)$ is a nondimensional, statistically derived chlorophyll-specific absorption coefficient; $a_w(\lambda)$ and $a_c^*(\lambda)$ are given in Table 3.7 of *Mobley* [1994]. The total scattering coefficient $b(z; \lambda)$ is obtained from the bio-optical model given by *Gordon and Morel* [1983]:

$$b(\lambda) = \left(\frac{550}{\lambda}\right) 0.30 C^{0.62}. \tag{40}$$

The phase function used is the same as in equation (31). The solar incidence is in the direction of 57°; the ratio of sky-total incident irradiance is 0.3 [*Mobley*, 1994]; and the ocean surface is assumed to be flat.

[29] Figure 2 shows the comparison between the present Monte Carlo model with that of *Mobley* [1994] in terms of downwelling and upwelling irradiance for the light wavelengths of $\lambda = 400$ nm, 500 nm, 600 nm, and 700 nm. It can be seen that the agreement is good.

3. Simulation Results

[30] From the LES, we obtain instantaneous, three-dimensional flow and scalar fields, based on which we perform MC simulations for the RTE. This paper focuses on the discussion of downwelling irradiance, $E_d(\mathbf{r}, t; \lambda)$, which is defined as

$$E_d(\mathbf{r}, t; \lambda) = \int_{\phi=0}^{2\pi} \int_{\theta=0}^{\pi/2} I(\mathbf{r}, t; \mathbf{\Omega}; \lambda) \, |\cos\theta| \, \mathrm{d}\Omega, \tag{41}$$

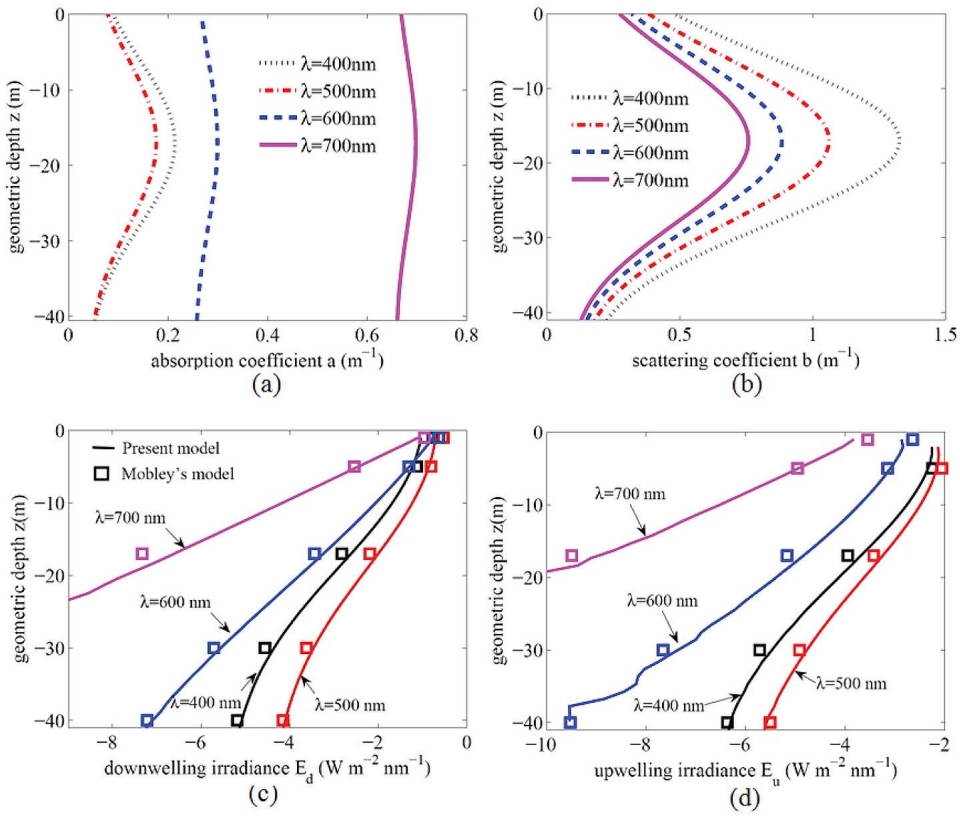

Figure 2. Comparison of the present Monte Carlo method with *Mobley* [1994]. Plotted are vertical profiles of (a) the absorption coefficient a, (b) the scattering coefficient b, (c) the downwelling irradiance E_d, and (d) the upwelling irradiance E_u. The results with different light wavelengths including λ = 400 nm (black), 500 nm (red), 600 nm (blue), and 700 nm (purple) are shown. In Figures 2c and 2 d: solid lines, the results of the present RT simulation; open squares, the data from the simulation of *Mobley* [1994].

where t is the time. Two statistical quantities are of particular interest to the study of the variations of downwelling irradiance, namely its mean value and the coefficient of variation. The mean value of E_d is defined as

$$\langle E_d \rangle(z;\lambda) = \frac{1}{L_t}\frac{1}{L_x L_y}\int_t \int_x \int_y E_d(\mathbf{r},t;\lambda)\,\mathrm{d}x\,\mathrm{d}y\,\mathrm{d}t, \tag{42}$$

where L_t is the duration of the simulation, and $L_x L_y$ is the area of the horizontal plane. Here and hereafter, $\langle\cdot\rangle$ denotes the averaged value. Accordingly, the coefficient of variation of E_d is defined as

$$CV_{Ed}(z;\lambda) = \frac{\left\langle [E_d(\mathbf{r},t;\lambda) - \langle E_d(z;\lambda)\rangle]^2 \right\rangle^{1/2}}{\langle E_d(z;\lambda)\rangle}. \tag{43}$$

[31] For the results shown below, for simplicity, we consider only the cases with the Sun's position at zenith and solar incidence normal to the ocean surface. It is assumed that at the bottom of the computational domain ($z = -100$ m, which we denote as the "deep region" in this study), the temperature and salinity have the asymptotic values of T_{deep} = 5°C and S_{deep} = 35 ppt, respectively. The differences in the temperature and salinity between the deep region and the sea surface play an important role in affecting the underwater light patterns and variations. A variety of surface values of T and S are considered, including T_{surface} = 10°C, 15°C, and 20°C and S_{surface} = 32 ppt, 32 ppt, and 34 ppt. Hereafter, we denote these cases as the temperature difference $\Delta T = T_{\mathrm{surface}} - T_{\mathrm{deep}}$ = 5°C, 10°C, and 15°C and the salinity difference $\Delta S = S_{\mathrm{deep}} - S_{\mathrm{surface}}$ = 1 ppt, 2 ppt, and 3 ppt. Note that here, the surface temperature is warmer than below, while the surface salinity is lower than below.

3.1. Under Calm Ocean Surface

[32] We first consider the case where the wave is absent to investigate the effect of the underwater turbulence. For the case of light wavelength λ = 500 nm, temperature difference ΔT = 15°C, and salinity difference ΔS = 2 ppt, the vertical profiles of the mean values and the coefficients of variation of the attenuation coefficient c and the single scattering albedo ω_0 are shown in Figure 3. From Figure 3a, we can see that as the location becomes deeper, $\langle c\rangle$ decreases while $\langle\omega_0\rangle$ increases. The majority of their change occurs near the sea surface over a depth of around 20 m. From Figure 3b, we can observe that CV_c and CV_{ω_0} are quite close to each other. Their maximum values are located very close to the sea surface.

[33] For the same case as above, Figure 4 shows an example of the instantaneous distributions of the attenuation coefficient c, single scattering albedo ω_0, and downwelling irradiance E_d on a horizontal plane that is 12.5 m below the ocean surface. Figure 4a shows that the horizontal variation of c is $O(10^{-3})$ m^{-1}. Figure 4b shows that the instantaneous

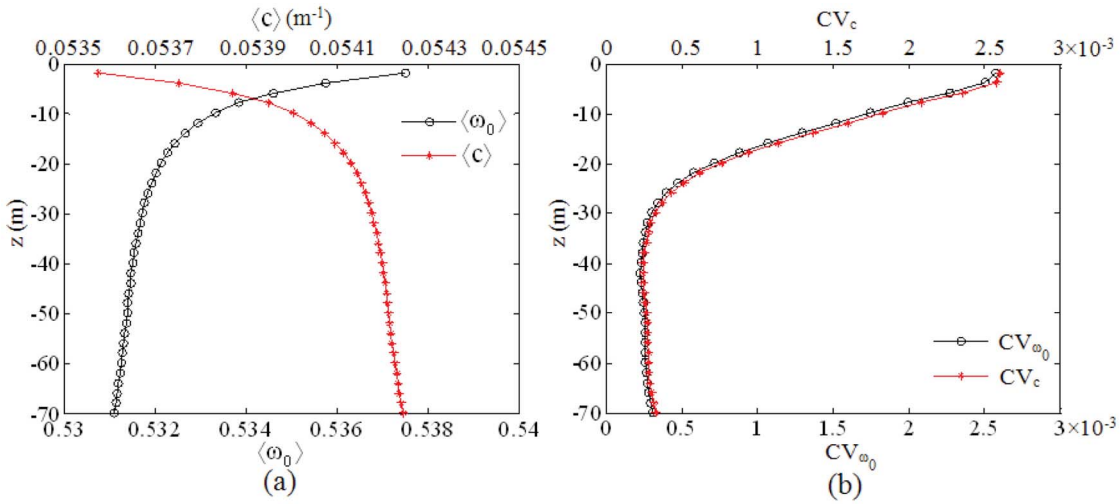

Figure 3. Vertical profiles of (a) the mean value and (b) the coefficient of variation of the attenuation coefficient c (black) and the scattering albedo ω_0 (red). The case with the light wavelength $\lambda = 500$ nm, the temperature difference $\Delta T = 15°$C, and the salinity difference $\Delta S = 2$ ppt is shown here.

ω_0 has a distribution pattern similar to that of c, and the magnitude of ω_0 variation is also small. The distribution of E_d (plotted in Figure 4c) has high correlation with those of c and ω_0 and, not surprisingly, the relative fluctuations of E_d is weak because the change in IOPs is small.

3.1.1. Turbulent Flow With and Without Turbulence Fluctuation

[34] In oceanic turbulent flows, temperature and salinity vary in the vertical direction due to the difference between their sea surface and deep region values, as well as in the horizontal directions due to turbulence fluctuations. We use numerical simulation to illustrate these two effects by considering two cases. The first case is the one discussed earlier, which has the light wavelength λ = 500 nm, temperature difference $\Delta T = 15°$C, and salinity difference $\Delta S = 2$ ppt in a turbulent flow under a calm ocean surface. The attenuation coefficient c and single scattering albedo ω_0 in this flow have the profiles of the mean values shown in Figure 3a and the profiles of the coefficients of variation shown in Figure 3b. The second case is an artificial one, which has the same vertical profiles of the mean IOPs as in the first case, but with the turbulence-induced horizontal fluctuations in the IOPs removed. That is, the second case has uniform IOPs in the horizontal directions.

[35] We perform MC simulations for the above two cases and plot the results in Figure 5. Figure 5a shows that these two cases have the almost identical vertical profiles of the mean E_d. This result indicates that the vertical structures of the mean IOPs, which are identical between the two cases, play a dominant role in the vertical variation of the irradiance on average. *Mobley* [1994] pointed out that "turbulence-induced scatter is unimportant in the overall redistribution of radiant energy in lakes and oceans." Our result is consistent with this statement as far as the mean irradiance is concerned. The turbulence effect is, on the other hand, manifested in the horizontal variation of E_d, which is quantified through CV_{Ed} and is plotted in Figure 5b. As shown, CV_{Ed} behaves differently between the two cases. For the second case in which the

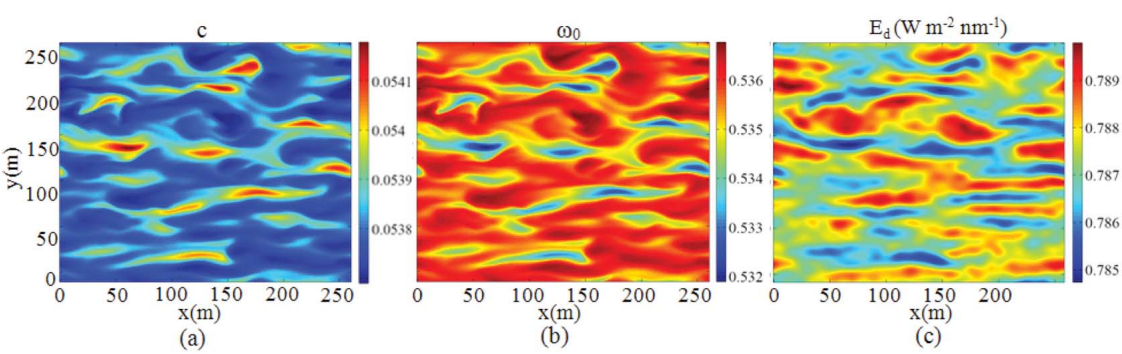

Figure 4. Instantaneous horizontal distributions of (a) the attenuation coefficient c, (b) the single scattering albedo ω_0, and (c) the downwelling irradiance E_d at the depth of 12.5 m. The case of calm ocean surface with the light wavelength $\lambda = 500$ nm, the temperature difference $\Delta T = 15°$C, and the salinity difference $\Delta S = 2$ ppt is shown here.

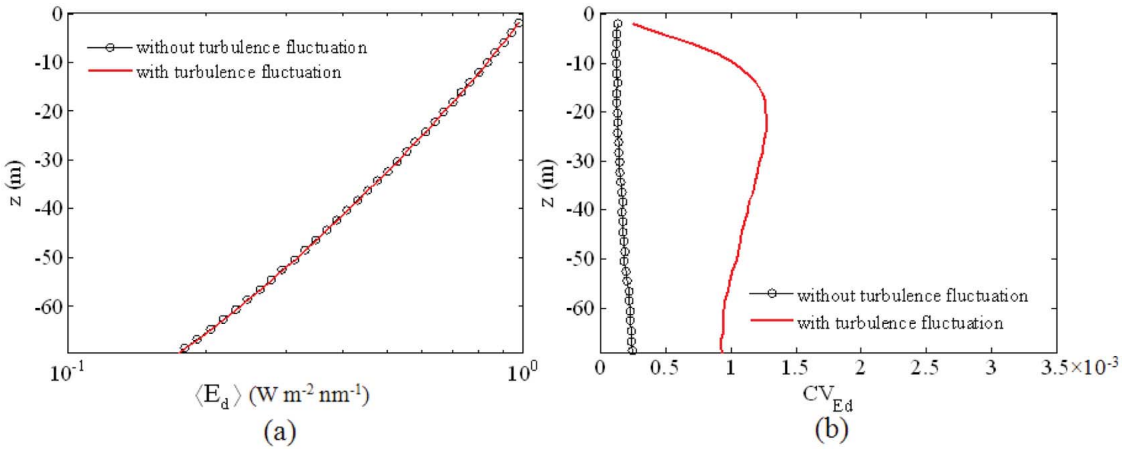

Figure 5. Vertical profiles of (a) the mean value and (b) the coefficient of variation of the downwelling irradiance E_d for the cases of with the consideration of turbulence fluctuation (red) and without the consideration of turbulence fluctuation (black). The case of calm ocean surface with the light wavelength $\lambda = 500$ nm, the temperature difference $\Delta T = 15°$C, and the salinity difference $\Delta S = 2$ ppt is shown here.

turbulence fluctuations are removed, CV_{Ed} is zero by definition. In the numerical result shown in Figure 5b, it has small values due to the numerical noise in MC simulation. Nevertheless, the noise magnitude is appreciably smaller than the CV_{Ed} value of the first case, which shows the turbulence effect. The figure also shows that in the turbulence case, away from the ocean surface, CV_{Ed} increases and reaches its maximum value around the depth of 20 m and then decreases. This result is consistent with the IOP variations depicted in Figure 3b, which has relatively large magnitude in the region of -20 m $\lesssim z \lesssim 0$ m. Below $z \sim -20$ m, the scattering effect, which reduces the variation of the light field, becomes more important, and CV_{Ed} decreases gradually when the depth increases.

3.1.2. Effects of Light Wavelength

[36] Lights of different wavelengths have different IOPs, which lead to different radiant energy distributions in oceanic turbulent flow. To illustrate this effect, we consider $\lambda = 400$ nm, 500 nm, and 600 nm. Based on section 2.2, we calculate the corresponding IOPs. On average, the attenuation coefficient $c \approx 0.0590$ m^{-1}, 0.0535 m^{-1}, and 0.595 m^{-1}, respectively, and the single scattering albedo $\omega_0 \approx 0.62$, 0.54, and 0.43, respectively. Mainly affected by ω_0, the cases of $\lambda = 400$ nm and 600 nm have respectively the slowest and fastest attenuation rates, as shown in Figure 6a.

[37] The coefficients of variation for the attenuation coefficient and single scattering albedo behave differently from their mean values. Using the parameterizations given in section 2.2, we found that the case of $\lambda = 400$ nm has the largest CV_c and CV_{ω_0} values among the three wavelengths, with the remaining two wavelengths having similar profiles of CV_c and CV_{ω_0} between them (not plotted here). As a result, as shown in Figure 6b, the coefficient of variation of downwelling irradiance is the largest for $\lambda = 400$ nm, and is similar between $\lambda = 500$ nm and 600 nm.

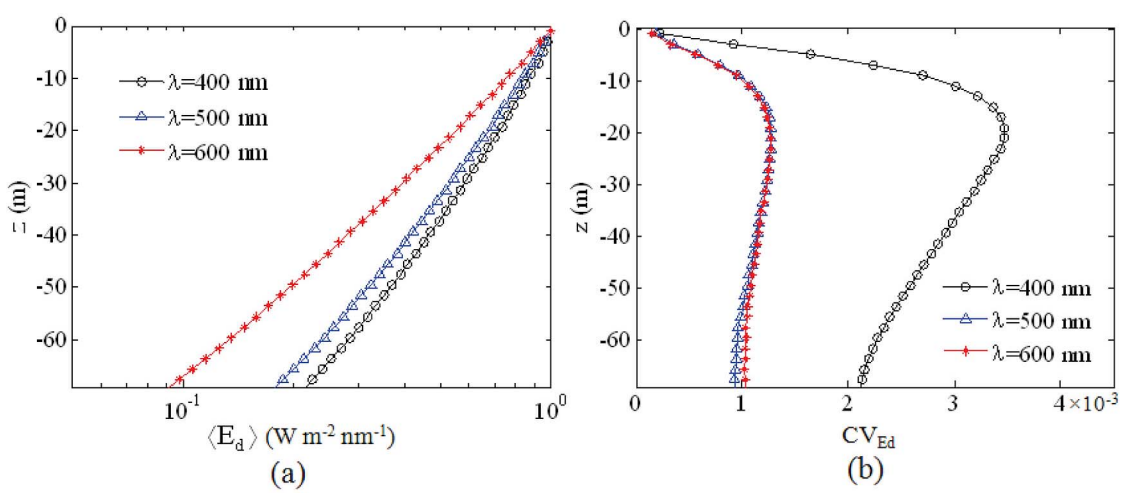

Figure 6. Vertical profiles of (a) the mean value and (b) the coefficient of variation of the downwelling irradiance E_d for different light wavelengths including $\lambda = 400$ nm (black), 500 nm (blue), and 600 nm (red). The case of calm ocean surface with the temperature difference $\Delta T = 15°$C and the salinity difference $\Delta S = 2$ ppt is shown.

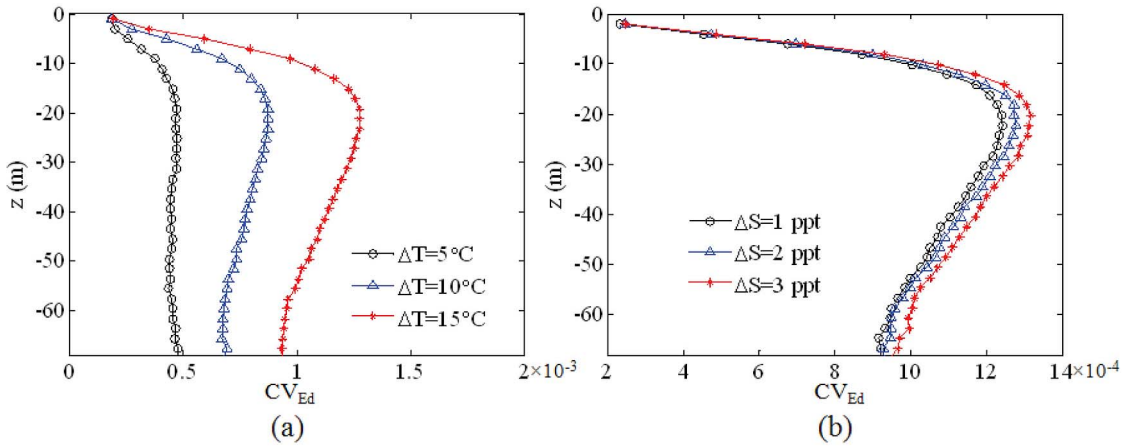

Figure 7. Vertical profiles of the coefficient of variation of the downwelling irradiance E_d for (a) salinity difference ΔS = 2 ppt and various values of temperature difference of ΔT = 5°C (black), 10°C (blue), and 15°C (red); and (b) temperature difference ΔT = 15°C and various values of salinity difference of ΔS = 1 ppt (black), 2 ppt (blue), and 3 ppt (red). The case of calm ocean surface with the light wavelength λ = 500 nm is shown here.

3.1.3. Effects of Temperature and Salinity Differences

[38] To understand how the differences in temperature and salinity between the sea surface and deep region affect the turbulence effect on the light field, we calculate a variety of cases with ΔT and ΔS varying independently.

[39] Assuming light wavelength λ = 500 nm, we first keep ΔS fixed at 2 ppt and consider ΔT = 5°C, 10°C, and 15°C, respectively. This corresponds to the typical ocean conditions of the deep ocean having temperature 5°C while the sea surface temperature ranges from 10°C to 20°C. Based on the parameterizations in section 2.2, for the temperature of 5°C, 10°C, 15°C, and 20°C, the attenuation coefficient c is respectively 0.0533 m^{-1}, 0.0534 m^{-1}, 0.0535 m^{-1}, and 0.0536 m^{-1}, and the single scattering albedo ω_0 is respectively 0.541, 0.540, 0.539, and 0.538. Due to the very small change in c and ω_0, it can be expected that the difference in the mean value of downwelling irradiance E_d is negligibly small among the different ΔT cases. The effect of ΔT is mainly manifested in the coefficient of variation of E_d, which is plotted in Figure 7a. As shown, relatively larger temperature difference leads to relatively bigger CV_{Ed}.

[40] We next consider the effect of salinity difference. Simulations with ΔT = 15°C and ΔS = 1 ppt, 2 ppt, and 3 ppt are performed. Because the variations of the mean values of c and ω_0 are small, the effect of ΔS on the mean values of E_d is almost indiscernible in our simulation results. The coefficients of variation of E_d for different ΔS are shown in Figure 7b. From the comparison between Figures 7a and 7b, it can be concluded that the influence of salinity fluctuations on the underwater light variation is weaker than that of temperature fluctuations.

3.2. Under Dynamic Ocean Surface Waves

[41] In this section, we discuss the cases in which the wave is present to investigate the combined effect of wave and turbulence on underwater irradiance. The majority of previous studies used linearization approximation at the ocean surface. It has been shown that with linearization approximation of the Snell's law, the power spectrum density of downwelling irradiance has a linear dependence on the spectra of surface elevation, surface slope, and surface curvature [*Walker*, 1994]. Recently, the downwelling irradiance has been found to be governed by a Poisson distribution with its mean value being a function of surface slope and surface curvature [*Shen et al.*, 2011].

[42] To illustrate the effect of surface deformation on the underwater light field, Figure 8 shows instantaneous surface elevation and downwelling irradiance on a horizontal plane below the surface for the case of light wavelength λ = 500 nm. The focusing and defocusing effect of the surface geometry on the underwater irradiance is clearly seen. Due to wave–turbulence interaction, the surface wave is distorted, which results in complex patterns in the underwater light field. In the case shown in Figures 8a and 8b, the wave and the turbulent shear flow are in the same direction. Compared with the case plotted in Figures 8c and 8d in which the wave and shear flow are in opposite directions, the first case has larger wave amplitude because of wave–turbulence interaction, and more coherent distribution of the underwater downwelling irradiance.

[43] The statistics of downwelling irradiance is shown in Figure 9. In addition to the above two cases, we also consider the scenario of having the wave only but without the turbulent shear flow. As shown in Figure 9a, the difference in the mean downwelling irradiance is small among these three cases. This similarity indicates that the averaged effect of light attenuation is governed by the mean IOPs, which have similar vertical variations among the three cases. Similar results are shown for the calm ocean surface cases discussed in section 3.1. The turbulence effect is manifested in the magnitude of horizontal variation of the downwelling irradiance. Due to the fluctuations in IOPs caused by turbulence and, more importantly, due to the distortion of the wave surface caused by wave–turbulence interaction, the CV_{Ed} profiles are different among the three cases as shown in Figure 9b. When the wave and turbulent shear flow are in opposite directions, CV_{Ed} has the largest magnitude, consistent with the observation in Figure 8d that the spatial

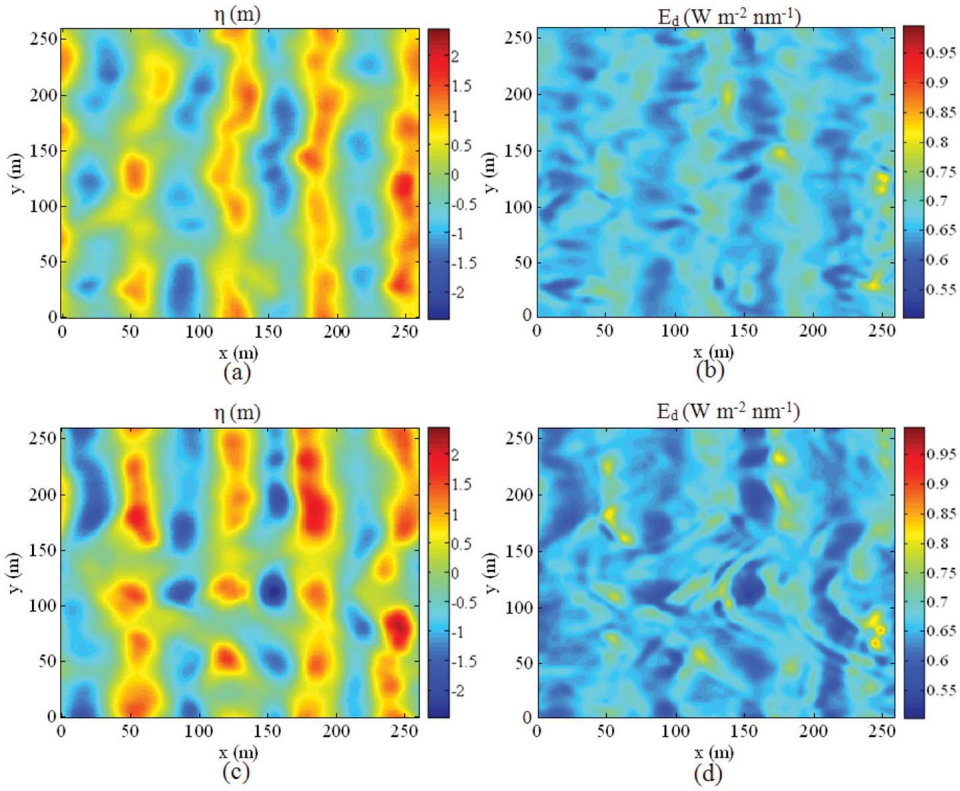

Figure 8. Instantaneous (a) sea surface elevation and (b) downwelling irradiance E_d at the depth of 12.5 m for the case that the surface wave and the shear flow are in the same direction; and instantaneous (c) sea surface elevation and (d) downwelling irradiance E_d at the depth of 12.5 m for the case that surface wave and the shear flow are in opposite directions. The case of the light wavelength $\lambda = 500$ nm, the temperature difference $\Delta T = 15°C$, the salinity difference $\Delta S = 2$ ppt, and the wave train with the initial amplitude $a^p = 1$ m is shown here.

variation of E_d is relatively larger compared with that in Figure 8c. If there exists wave only, Figure 9c shows that CV_{Ed} has smaller magnitude compared with the turbulence case, indicating the turbulence effect. We also note that in our results, the maxima of CV_{Ed} occur at a depth around 60 m, which is shallower than the focal point discussed by *Zaneveld and Hwang* [2001]. This discrepancy is associated with the scattering by ocean particles. Moreover, the wave

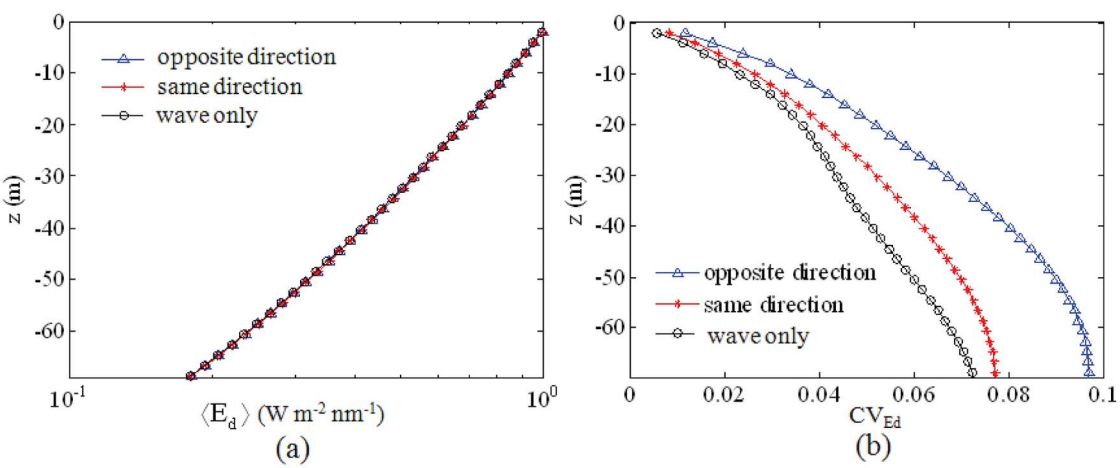

Figure 9. Vertical profiles of (a) the mean value and (b) the coefficient of variation of the downwelling irradiance E_d for the cases in which the surface wave and shear flow are in the opposite (blue) and the same (red) directions as well as the case with a wave train but without turbulence (black). The cases with the light wavelength $\lambda = 500$ nm, the temperature difference $\Delta T = 15°C$, the salinity difference $\Delta S = 2$ ppt, and the wave train with the initial amplitude $a^p = 1$ m are shown here.

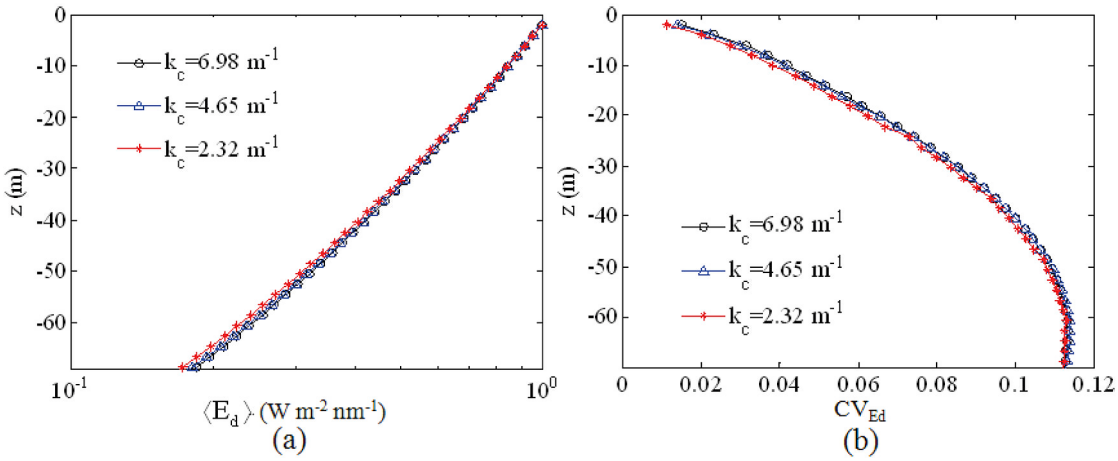

Figure 10. Vertical profiles of (a) the mean value and (b) the coefficient of variation of the downwelling irradiance E_d with different cut-off wavenumbers in the sea surface elevation presentation: k_c = 6.98 m^{-1} (black), 4.65m^{-1} (blue), and 2.32m^{-1} (red). The cases with the light wavelength λ = 500 nm, the temperature difference ΔT = 15°C, the salinity difference ΔS = 2 ppt, and the wave train with the initial amplitude a^p = 1.5 m are shown here.

surface modulation due to wave–turbulence interaction, which is captured directly in our fully-nonlinear dynamic ocean surface calculation, also affects the location of the maximum variation of E_d.

[44] Finally, to show that the resolution of our simulation is adequate, we plot in Figure 10 the results of $\langle E_d \rangle$ and CV_{Ed} profiles with different cut-off wavenumbers, k_c, of the ocean surface representation. The results shown in previous figures all have k_c = 4.65 m^{-1}. When the resolution is increased to k_c = 2.32 m^{-1} or decreased to k_c = 6.98 m^{-1}, Figure 10 shows that the difference in the simulation results is negligibly small, indicating the adequacy of the simulation resolution used in this study.

4. Conclusions and Discussion

[45] In this study, we have numerically studied the effects of turbulence in the upper ocean on the underwater irradiance. We obtained the ocean turbulence data by performing large-eddy simulations. We quantified the turbulence structures of IOPs with empirical models for the dependence of IOPs on temperature and salinity. We then used a Monte Carlo method to simulate the radiative transfer process in the turbulence field, and quantified the natural solar light distribution inside the inhomogeneous ocean body.

[46] With the simulation data, we have investigated the effect of oceanic turbulence on the statistics of underwater light field in terms of the mean value and the coefficient of variation of downwelling irradiance. A variety of flow, temperature, and salinity conditions are examined. It is found that the vertical profile of the mean downwelling irradiance is mainly determined by the vertical structure of the mean values of IOPs. Turbulence effect is manifested in the horizontal variation of the downwelling irradiance, which correlates with the variations of the attenuation coefficient and single scattering albedo. This effect is illustrated by simulations of different light wavelengths which have different IOPs. It is also found that the relative magnitude of downwelling irradiance variation is largely affected by the differences in the temperature and salinity between the sea surface and the deep region, because the differences determine the magnitude of IOP variations. Under typical ocean conditions, between the temperature and salinity, the former has a relatively stronger effect on the irradiance than the latter does. In the presence of ocean surface waves, the horizontal variation of downwelling irradiance is enhanced due to surface deformation, which is largely affected by wave–turbulence interaction.

[47] From this study, it is shown that oceanic turbulence induces variations in temperature and salinity and modulates the wave surface through wave–turbulence interaction. The variation in the underwater irradiance field due to the turbulence-induced IOP change inside the ocean body has small magnitude. As such, measurement instruments need to have high resolutions to capture such phenomenon. On the other hand, from Figure 4, we see that high correlation exists between the downwelling irradiance and oceanic IOPs. If high-quality underwater irradiance measurement is available, using the relations between IOPs and temperature and salinity, one may be able to deduce the frequency spectra of temperature and salinity in the ocean by measuring the time series of downwelling irradiance.

[48] We note that the present simulation approach is employed because the light source in question is the incoherent solar light. Therefore, the radiative transfer equation is chosen over the Maxwell's equations for the purpose of obtaining underwater radiant energy distribution. We also note that in this study, the chlorophyll concentration is assumed to be constant along the depth and thus does not fluctuate with turbulence. For some other applications, the mixing of chlorophyll by oceanic turbulence plays an important role in the underwater radiative transfer. The present numerical simulation approach can be extended to these applications, if the chlorophyll transport and other processes, such as the interaction with nutrients and the photosynthetically active radiation, are included to the computational framework.

[49] **Acknowledgments.** This study was supported by the Office of Naval Research through the Radiance in a Dynamic Ocean (RaDyO) project. The computing resources were provided by the Department of Defence high-performance computing modernization program (HPCMP). We thank Yuming Liu, Di Yang, and Meng Shen for their helpful discussions during the course of this study.

References

Adams, J. T., and D. J. Gray (2011), Neutral points in an atmosphere-ocean system. 2: Downwelling light field, *Appl. Opt.*, *50*, 335–345.

Austin, R. W., and G. Halikas (1976), The index of refraction of seawater, *SIO Ref. 76-1*, Scripps Inst. of Oceanogr., La Jolla, Calif.

Bal, G. (2006), Radiative transfer equations with varying refractive index: A mathematical perspective, *J. Opt. Soc. Am. A*, *23*, 1639–1643.

Bogucki, D. J., J. A. Domaradzki, D. Stramski, and J. R. Zaneveld (1998), Comparison of near-forward light scattering on oceanic turbulence and particles, *Appl. Opt.*, *37*, 4669–4776.

Bogucki, D. J., J. A. Domaradzki, R. E. Ecke, and C. R. Truman (2004), Light scattering on oceanic turbulence, *Appl. Opt.*, *43*, 5662–5668.

Bogucki, D. J., J. A. Domaradzki, C. Anderson, H. W. Wijesekera, J. R. V. Zaneveld, and C. Moore (2007a), Optical measurement of rates of dissipation of temperature variance due to oceanic turbulence, *Opt. Express*, *15*(12), 7224–7230.

Bogucki, D. J., J. Piskozub, M.-E. Carr, and G. D. Spiers (2007b), Monte Carlo simulation of propagation of a short light beam through turbulent oceanic flow, *Opt. Express*, *15*(21), 13,988–13,996.

Born, M., and E. Wolf (1970), *Principles of Optics*, Oxford, U. K.

Bou-Zeid, E., C. Meneveau, and M. B. Parlange (2004), Large-eddy simulation of neutral atmospheric boundary layer flow over heterogeneous surfaces: Blending height and effective surface roughness, *Water Resour. Res.*, *40*, W02505, doi:10.1029/2003WR002475.

Bou-Zeid, E., C. Meneveau, and M. B. Parlange (2005), A scale-dependent Lagrangian dynamic model for large eddy simulation of complex turbulent flows, *Phys. Fluids*, *17*, 025105, doi:10.1063/1.1839152.

Bricaud, A., M. Babin, A. Morel, and H. Claustre (1995), Variability in the chlorophyll-specific absorption coefficients of natural phytoplankton: Analysis and parameterization, *J. Geophys. Res.*, *100*, 13,321–13,332.

Chamecki, M., C. Meneveau, and M. B. Parlange (2008), A hybrid spectral/finite-volume algorithm for large-eddy simulation of scalars in the atmospheric boundary layer, *Boundary Layer Meteorol.*, *128*, 473–484.

Chilton, F., D. D. Jones, and W. K. Talley (1969), Imaging properties of light scattered by the sea, *J. Opt. Soc. Am.*, *59*, 891–898.

Dera J., and D. Stramski (1986), Maximum effects of sunlight focusing under a wind-disturbed sea surface, *Oceanologia*, *23*, 15–42.

Dimas, A. A., and Triantafyllou, G. S. (1994), Nonlinear interaction of shear flow with a free surface, *J. Fluid Mech.*, *260*, 211–246.

Duntley, S. Q. (1974), Underwater visbility and photography, in *Optical Aspects of Oceanography*, edited by N. G. Jerlov and E. S. Nielsen, pp. 135–149, Academic, New York.

Germano, M., U. Piomelli, P. Moin and W. H. Cabot (1991), A dynamic subgrid-scale eddy viscosity model, *Phys. Fluids*, *3*, 1760–1765.

Gernez, P., and D. Antoine (2009), Field characterization of wave-induced underwater light field fluctuations, *J. Geophys. Res.*, *114*, C06025, doi:10.1029/2008JC005059.

Gilbert, G. D., and R. C. Honey (1972), Optical turbulence in the sea, in *Underwater Photo-Optical Instrumentation Applications*, *Proc. SPIE*, *24*, 49–55.

Gordon, H. R., and A. Morel (1983), *Remote Assessment of Ocean Color for Interpretation of Satellite Visible Imagery: A Review*, *Lecture Notes Coastal Estuarine Stud.*, vol. 4, 114 pp., Springer, New York.

Guo, X., and L. Shen (2009), On the generation and maintenance of waves and turbulence in simulations of free-surface turbulence, *J. Comput. Phys.*, *228*, 7313–7332.

Guo, X., and L. Shen (2010), Interaction of a deformable free surface with statistically steady homogeneous turbulence, *J. Fluid Mech.*, *658*, 33–62.

Haltrin, V. I. (1998), One-parameter model of seawater optical properties, paper presented at Ocean Optics XIV Conference, Off. of Nav. Res., Kailua-Kona, Hawaii.

Handler, R. A., J. R. Saylor, R. I. Leighton, and A. L. Rovelstad (1999), Transport of a passive scalar at a shear-free boundary in fully developed turbulent open channel flow, *Phys. Fluids*, *11*, 2607–2625.

Hansen, D. V., and W. C. Thacker (1999), Estimation of salinity profiles in the upper ocean, *J. Geophys. Res.*, *104*, 7921–7933.

Honey, R. C., and G. P. Sorenson (1970), Optical absorption and turbulence-induced narrow-angle forward scatter in the sea, *AGARD Conf. Proc.*, *77*, 39.1–39.7.

Kermani, A., H. R. Khakpour, L. Shen, and T. Igusa (2011), Statistics of surface renewal of passive scalars in free-surface turbulence, *J. Fluid Mech.*, *678*, 379–416.

Khakpour, H. R., L. Shen, and D. K. P. Yue (2011), Transport of passive scalar in turbulent shear flow under a clean or surfactant-contaminated free surface, *J. Fluid Mech.*, *670*, 527–557.

Kim, J., and P. Moin (1985), Application of a fractional-step method to incompressible Navier–Stokes equations, *J. Comput. Phys.*, *59*, 308–323.

Kopelevich, O. V. (1983), Small-parametric model of the optical properties of seawater, in *Ocean Optics I*, pp. 208–234, Nauka, Moscow.

Korotkova, O., and N. Farwell (2011), Effect of oceanic turbulence on polarization of stochastic beams, *Opt. Commun.*, *284*, 1740–1746.

Lewis, M. R., J. J. Cullen, and T. Platt (1983), Phytoplankton and thermal structure in the upper ocean: Consequences of nonuniformity in chlorophyll profile, *J. Geophys. Res.*, *88*, 2565–2570.

Lilly, D. K. (1992), A proposed modification of the German subgrid-scale closure method, *Phys. Fluids*, *4*, 633–635.

Lu, W., L. Liu, and J. Sun (2006), Influence of temperature and salinity fluctuations on propagation behaviour of partially coherent beams in oceanic turbulence, *J. Opt. A*, *8*, 1052–1058.

McNeil, G. T. (1977), Metrical fundamentals of underwater lens system, *Opt. Eng.*, *16*, 128–139.

Meneveau, C., and J. Katz (2000), Scale-invariance and turbulence models for large-eddy simulation, *Annu. Rev. Fluid. Mech.*, *32*, 1–32.

Meneveau, C., T. S. Lund, and W. H. Cabot (1996), A Lagrangian dynamic subgrid-scale model of turbulence, *J. Fluid Mech.*, *319*, 353–385.

Mobley, C. D. (1994), *Light and Water: Radiative Transfer in Natural Water*, Academic, San Diego, Calif.

Morel, A. (1991), Light and marine photosynthesis: A spectral model with geochemical and climatological implications, *Prog. Oceanogr.*, *26*, 263–306.

Morel, A., and L. Prieur (1977), Analysis of variations in oceann color, *Limnol. Oceanogr.*, *22*, 709–722.

Nikishov, V. V., and V. I. Nikishov (2000), Spectrum of turbulent fluctuations of the sea-water refraction index, *Int. J. Fluid Mech. Res.*, *27*, 82–98.

Pegau, W. S., D. Gray, and J. R. V. Zaneveld (1997), Absorption and attenuation of visible and near-infrared light in water: Dependence on temperature and salinity, *Appl. Opt.*, *36*, 6035–6046.

Petzold, T. J. (1972), Volume scattering functions for selected ocean water, *SIO Ref. 72-78*, Scripps Inst. of Oceanogr., La Jolla, Calif.

Pope, R. M., and E. S. Fry (1997), Absorption spectrum (380–700 nm) of pure water. II. Integrating cavity measurements, *Appl. Opt.*, *36*, 8710–8722.

Porté-Agel, F., C. Meneveau, and M. B. Parlange (2000), A scale-dependent dynamic model for large-eddy simulation: Application to a neutral atmospheric boundary layer, *J. Fluid Mech.*, *415*, 261–284.

Premaratne, M., E. Premaratne, and A. J. Lowery (2005), The photon transport equation for turbid biological media with spatially varying isotropic refractive index, *Opt. Express*, *13*, 389–399.

Quan, X., and E. S. Fry (1995), Empirical equation for the index of refraction of seawater, *Appl. Opt.*, *34*, 3477–3480.

Sagaut, P. (2006), *Large Eddy Simulation for Incompressible Flows*, Springer, New York.

Shen, L., and D. K. P. Yue (2001), Large-eddy simulation of free-surface turbulence, *J. Fluid Mech.*, *440*, 75–116.

Shen, L., G. S. Triantafyllou, and D. K. P. Yue (2000), Turbulent diffusion near a free surface, *J. Fluid Mech.*, *407*, 145–166.

Shen, L., G. S. Triantafyllou, and D. K. P. Yue (2001), Mixing of a passive scalar near a free surface, *Phys. Fluids*, *13*, 913–926.

Shen, L., D. K. P. Yue, and G. S. Triantafyllou (2004), Effect of surfactants on free-surface turbulent flows, *J. Fluid Mech.*, *506*, 79–115.

Shen, M., Z. Xu, and D. K. P. Yue (2011), A model for the probability density function of downwelling irradiance under ocean waves, *Opt. Express*, *19*(18), 17,528–17,538.

Shendeleva, M. L., and J. A. Molloy (1999), Scaling property of the diffusion equation for light in a turbid medium with varying refractive index, *J. Opt. Soc. Am. A*, *24*, 2902–2910.

Skamarock, W. C. (2006), Positive-definite and monotonic limiters for unrestricted-time-step transport schemes, *Mon. Weather Rev.*, *134*, 2241–2250.

Skamarock, W. C., and M. L. Weisman (2009), The impact of positive-definite moisture transport on NWP precipitation forecasts, *Mon. Weather Rev.*, *137*, 488–494.

Smagorinsky, J. (1963), General circulation experiments with the primitive equations. I. The basic experiment, *Mon. Weather Rev.*, *91*, 99–163.

Snyder R. L., and J. Dera (1970), Wave-induced light-field fluctuations in sea, *J. Opt. Soc. Am. B*, *60*(8), 1072–1083.

Stramski, D., and L. Legendre (1992), Laboratory simulation of light focusing by water usrface waves, *Mar. Biol.*, *114*, 341–348.
Triantafyllou, G. S., and A. A. Dimas (1989), Interaction of two-dimensional seperated flows with a free surface at low Froude numbers, *Phys. Fluids*, *1*, 1813–1821.
Tualle, J.-M., and E. Tinet (2003), Derivation of the radiative transfer equation for scattering media with a spatially varying refractive index, *Opt. Commun.*, *228*, 33–38.
Walker, R. E. (1994), *Marine Light Field Statistics*, Wiley-Interscience, Hoboken, N. J.
Wang, H., W. C. Skamarock, and G. Feingold (2009), Evaluation of scalar advection schemes in the advanced research WRF model using large-eddy simulations of aerosol–cloud interactions, *Mon. Weather Rev.*, *137*, 2547–2558.
Yang, D., and L. Shen (2011a), Simulation of viscous flows with undulatory boundaries: Part I. Basic solver, *J. Comput. Phys.*, *230*, 5488–5509.
Yang, D., and L. Shen (2011b), Simulation of viscous flows with undulatory boundaries: Part II. Coupling with other solvers for two-fluid computation, *J. Comput. Phys.*, *230*, 5510–5531.
You Y., D. Stramski, M. Darecki, and G. W. Kattawar (2009), Modeling of wave-induced irradiance fluctuations at near-surface depths in the ocean: A comparison with measurements, *Appl. Opt.*, *49*(6), 1041–1053.
Zalesak, S. T. (1979), Fully multidimensional flux-corrected transport algorithms for fluids, *J. Comput. Phys.*, *31*, 335–362.
Zaneveld J. R. V., and P. A. Hwang (2001), The influence of coherent waves on the remotely sensed reflectance, *Opt. Express*, *9*(6), 260–266.
Zhang, X., L. Hu, and M.-X. He (2009), Scattering by pure seawater: Effect of salinity, *Opt. Express*, *17*, 5698–5710.

X. Guo and L. Shen, Department of Civil Engineering, Johns Hopkins University, Baltimore, MD 21218, USA.
Z. Xu and D. K. P. Yue, Department of Mechanical Engineering, Massachusetts Institute of Technology, Cambridge, MA 02139, USA. (yue@mit.edu)